Forming-free bipolar resistive switching in nonstoichiometric ceria films

Muhammad Ismail[1,3], Chun-Yang Huang[1], Debashis Panda[1], Chung-Jung Hung[2], Tsung-Ling Tsai[1], Jheng-Hong Jieng[1], Chun-An Lin[1], Umesh Chand[1], Anwar Manzoor Rana[3], Ejaz Ahmed[3], Ijaz Talib[3], Muhammad Younus Nadeem[3] and Tseung-Yuen Tseng[1*]

Abstract

The mechanism of forming-free bipolar resistive switching in a $Zr/CeO_x/Pt$ device was investigated. High-resolution transmission electron microscopy and energy-dispersive spectroscopy analysis indicated the formation of a ZrO_y layer at the Zr/CeO_x interface. X-ray diffraction studies of CeO_x films revealed that they consist of nano-polycrystals embedded in a disordered lattice. The observed resistive switching was suggested to be linked with the formation and rupture of conductive filaments constituted by oxygen vacancies in the CeO_x film and in the nonstoichiometric ZrO_y interfacial layer. X-ray photoelectron spectroscopy study confirmed the presence of oxygen vacancies in both of the said regions. In the low-resistance ON state, the electrical conduction was found to be of ohmic nature, while the high-resistance OFF state was governed by trap-controlled space charge-limited mechanism. The stable resistive switching behavior and long retention times with an acceptable resistance ratio enable the device for its application in future nonvolatile resistive random access memory (RRAM).

Keywords: Resistive switching; Space charge-limited conduction (SCLC); Metal-insulator-metal structure; Cerium oxide; Oxygen vacancy

Background

A metal-insulator-metal (MIM) structure-based resistive random access memory (RRAM) device has attracted much attention for next-generation high-density and low-cost nonvolatile memory applications due to its long data retention, simple structure, high-density integration, low-power consumption, fast operation speed, high scalability, simple constituents, and easy integration with the standard metal oxide semiconductor (MOS) technology [1]. In addition to transition metal oxide-based RRAMs [2,3], many rare-earth metal oxides, such as Lu_2O_3, Yb_2O_3, Sm_2O_3, Gd_2O_3, Tm_2O_3, Er_2O_3, Nd_2O_3, Dy_2O_3, and CeO_2 [4-10], show very good resistive switching (RS) properties. Among them, CeO_2 thin films having a strong ability of oxygen ion or oxygen vacancy migration attract a lot of attention for RRAM applications [8-10]. CeO_2 is a well-known rare-earth metal oxide with a high dielectric constant (26), large bandgap (6 eV), and high refractive index (2.2 to 2.3). The cerium ion in the CeO_2 film exhibits both +3 and +4 oxidation states, which are suitable for valency change switching process [11,12]. Forming-free resistive switching and its conduction mechanism are very important for nonvolatile memory applications. In addition, oxygen vacancies or ions play a unique role in the resistive switching phenomenon [13]. Therefore, CeO_2 is expected to have potentials for applications in nonvolatile resistive switching memory devices [14]. However, there are quite limited reports on the resistive switching properties of CeO_2.

Here, we report the forming-free bipolar resistive switching properties of a nonstoichiometric CeO_x film having a $Zr/CeO_x/Pt$ device structure. The effect of the Zr top electrode on the resistive switching behavior of the CeO_x film is investigated. It is expected that the Zr top electrode reacts with the CeO_x layer and forms an interfacial ZrO_y layer. This reaction may be responsible for creating a sufficient amount of oxygen vacancies required for the formation and rupture of conductive filaments for resistive switching. In this study, we have found that the CeO_x-based RRAM device exhibits good

* Correspondence: tseng@cc.nctu.edu.tw
[1]Department of Electronics Engineering and Institute of Electronics, National Chiao Tung University, Hsinchu 30010, Taiwan
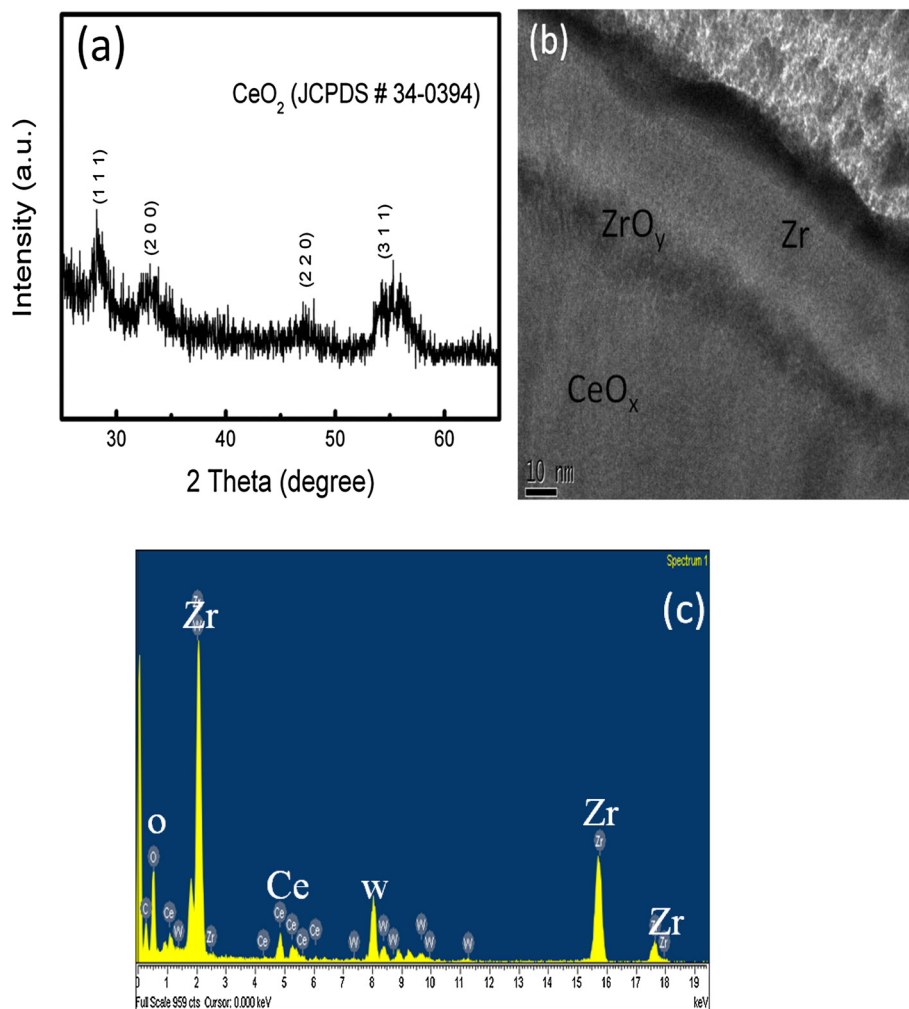Full list of author information is available at the end of the article

switching characteristics with reliable endurance and data retention, suitable for future nonvolatile memory applications.

Methods

A 200-nm-thick silicon dioxide (SiO_2) layer was thermally grown on a (100)-oriented p-type Si wafer substrate. Next, a 50-nm-thick Pt bottom electrode was deposited on a 20-nm-thick Ti layer by electron beam evaporation. The 14- to 25-nm-thick CeO_x films were deposited on Pt/Ti/SiO$_2$/Si at room temperature with a gas mixture of 6:18 Ar/O$_2$ by radio-frequency (rf) magnetron sputtering using a ceramic CeO_2 target. Prior to rf sputtering at 10-mTorr pressure and 100-W power, the base pressure of the chamber was achieved at 1.2×10^{-6} Torr. Finally, a 30-nm-thick Zr top electrode (TE) and a 20-nm-thick W TE capping layer were deposited by direct current (DC) sputtering on the CeO_x film through metal shadow masks having 150-μm diameters to form a sandwich MIM structure. The W layer was used to avoid the oxidation of the Zr electrode during testing. Structural and compositional characteristics of the CeO_x films were analyzed by X-ray diffraction (XRD; Bede D1, Bede PLC, London, UK) and X-ray photoelectron spectroscopy (XPS; ULVAC-PHI Quantera SXM, ULVAC-PHI, Inc., Kanagawa, Japan) measurements. The film thickness and interfacial reaction between Zr and CeO_x were confirmed by high-resolution cross-sectional transmission electron microscopy (HRTEM). Elemental presence of deposited layers was investigated by energy-dispersive spectroscopy (EDX). Electrical current–voltage (*I-V*) measurement was carried out using the Agilent B1500A (Agilent Technologies, Santa Clara, CA, USA) semiconductor analyzer characterization system at room temperature. During electrical tests, bias polarity was defined with reference to the Pt bottom electrode.
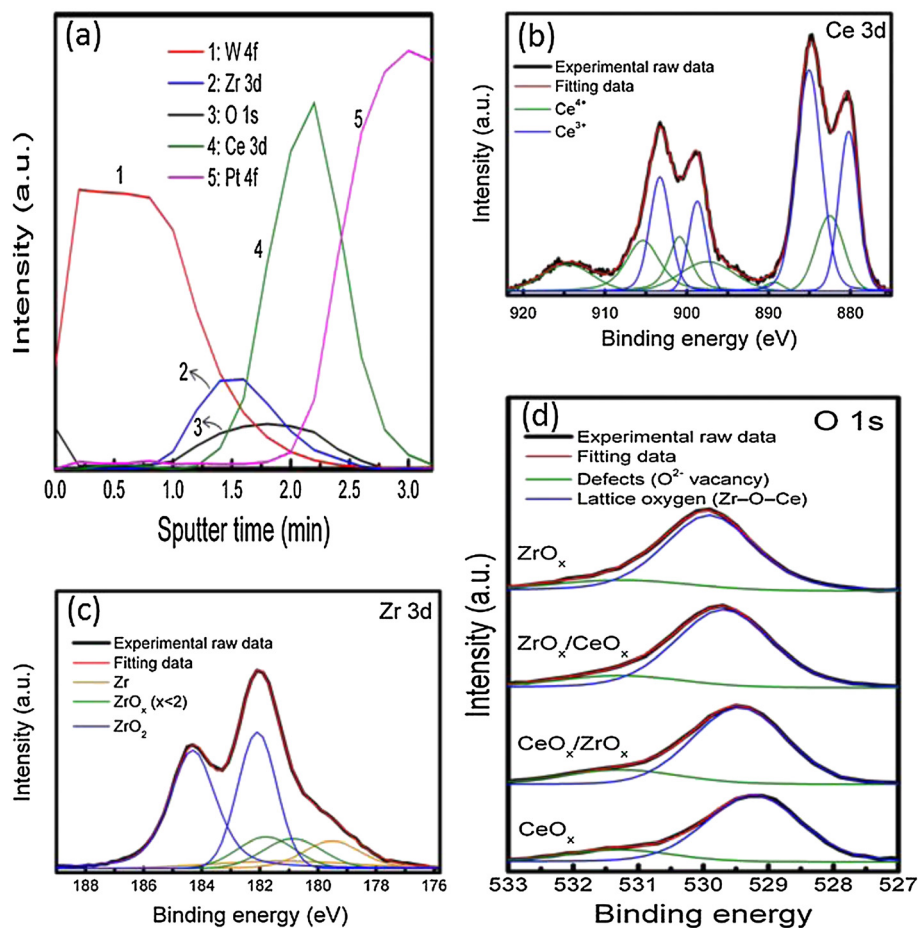

Figure 1 XRD pattern of the CeO$_x$ film and cross-sectional TEM and EDX images of the Zr/CeO$_x$/Pt device. (a) XRD pattern of the CeO$_x$ film deposited on Si wafer at room temperature. **(b)** Cross-sectional TEM image of the Zr/CeO$_x$/Pt device. **(c)** EDX image of the Zr/CeO$_x$/Pt device.
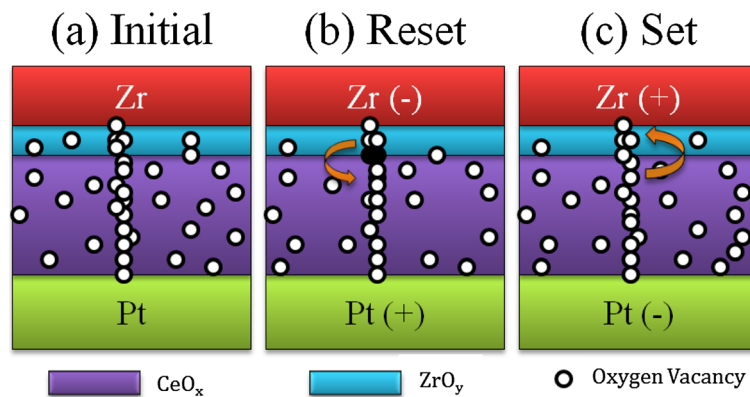
Results and discussion

Figure 1a shows the grazing angle (3°) XRD spectra of the CeO_x thin film deposited on Si (100) substrate. It indicates that the CeO_x film possesses a polycrystalline structure having (111), (200), (220), and (311) peaks, corresponding to the fluorite cubic structure (JCPDS ref. 34–0394). From the XRD analysis, the broad and wide diffraction peaks demonstrate that the CeO_x film exhibits poor crystallization. This could be due to the small thickness (approximately 14 nm) of the film. Figure 1b shows the cross-sectional HRTEM image of the $Zr/CeO_x/$ Pt device, which indicates that the ZrO_y layer is formed between CeO_x and Zr interfaces. Figure 1c depicts the EDX spectra of the CeO_x film. The elemental composition of the $Zr/CeO_x/Pt$ was determined by energy dispersion. The results from the EDX analysis that showed the main component present in this structure were O (38.41%), Zr (34. 05%), and Ce (3.83%). An oxygen peak at about 0.52 keV and Zr peaks at about 22.5 and 15.60 keV can be observed in the spectra.

The ZrO_y layer is also observed from XPS signals at the interface of Zr and CeO_2 layers. XPS analysis was carried out to examine the surface chemical composition and the valence/oxidation states of Ce and Zr species involved in the device by inspecting the spectral line shape and signal intensities associated with the core-level electrons. Figure 2a shows the depth profile of chemical composition in the $Zr/CeO_x/Pt$ device. The interdiffusion of O, Ce, and Zr atoms are evident from the spectra. This is an indication of the formation of an interfacial ZrO_y layer between the CeO_x and Zr top electrode. The formation of the ZrO_y layer is further confirmed from the shifting of Zr 3d peaks from a higher binding energy position to lower ones (Figure 2c). The CeO_x 3d spectrum shown in Figure 2b consists of two sets of spin-orbit multiplets. These multiplets are the characteristics of $3d_{3/2}$ and $3d_{5/2}$ (represented as u and v, respectively) [15]. The spin-orbit splitting is about 18.4 eV. The highest peaks at around 880.2 and 898.7 eV, recognized as v_0 and u_0 respectively, correspond to Ce^{3+} with the highest satellites as v'

Figure 2 XPS binding energy profiles. (a) Depth profiles of Zr, Ce, O, Pt, and W for the $W/Zr/CeO_x/Pt$ structure, **(b)** Ce 3d, **(c)** Zr 3d, and **(d)** O 1 s in the $Zr/CeO_x/Pt$ device.
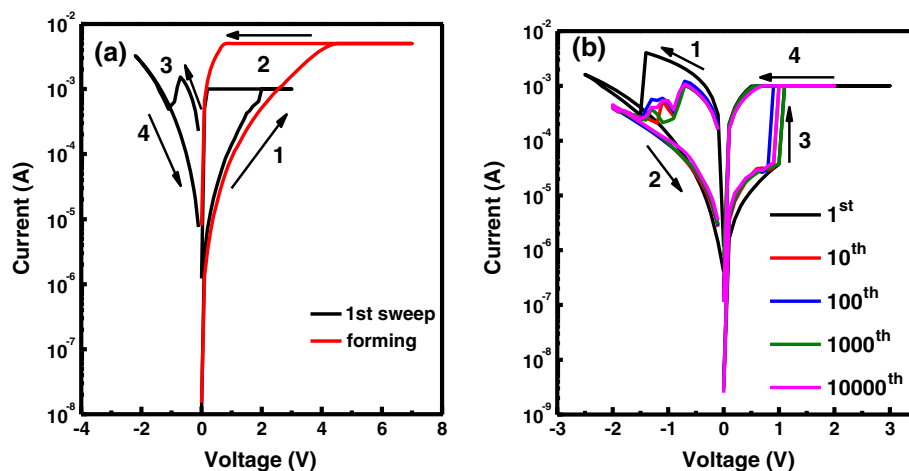
Figure 3 Schematic of oxygen vacancy-formed multiconducting filaments depicting the switching process in Zr/CeO$_x$/Pt device.
(a) Initial, (b) reset, and (c) set states. Note that unfilled (filled) circles represent oxygen vacancies (ions) in the CeO$_x$ films.
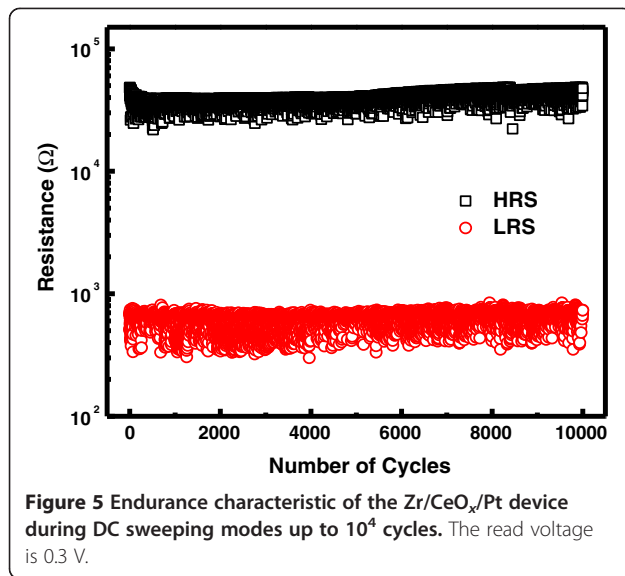
(885.1 eV) and u' (903.3 eV). Low-intensity peaks, i.e., v (882.5 eV) and u (900.9 eV) along with satellite features represented as v'' (889.4 eV), v''' (897.5 eV), u'' (905.4 eV), and u''' (914.6 eV), are observed, corresponding to the Ce^{4+} state.

In reference to the differentiation between the Ce^{3+} and Ce^{4+} species with different line shapes, the XPS spectra correspond to various final states: Ce(III) $= v_0 + v' + u_0 + u'$ and Ce(IV) $= v + v'' + v''' + u + u'' + u'''$ [16]. The presence of the Ce^{4+} state is normally supported by the intensity of the u''' peak, which is known as a fingerprint of Ce(IV) states [16]. This result implies that both Ce^{4+} and Ce^{3+} ions coexist in the bulk as well as in the surface of the CeO$_x$ film. Concentrations of Ce^{4+} and Ce^{3+}, as obtained from the deconvoluted XPS spectra, are 39.6% and 60.4%, respectively. The higher percentage of Ce^{3+} ions indicates that the film is rich of oxygen vacancies [17]. The XPS spectra of Zr 3d exhibit a doublet located at 184.3 and

182.08 eV, as shown in Figure 2c. This doublet corresponds to Zr 3d$_{3/2}$ and Zr 3d$_{5/2}$, respectively [18], as the final states of ZrO$_2$. Furthermore, the weak bands at about 181.7 eV assigned to Zr 3d$_{3/2}$ and 180.8 eV assigned to Zr 3d$_{5/2}$ seem to be consistent with the states of ZrO$_y$ ($0 < y < 2$, 181.6 eV) [19], which also provide an evidence of the formation of a ZrO$_y$ interfacial layer. Final states of the metallic Zr (3d) are evidenced by the weakest band at 181.2 eV for Zr 3d$_{3/2}$ and 179.5 eV for Zr 3d$_{5/2}$. Figure 2d displays the O 1 s XPS spectra of the Zr/CeO$_x$/Pt device consisting of peaks at binding energies 529.05, 530.09, and 531.47 eV, which can be attributed to the absorbed oxygen [20], lattice oxygen in CeO$_2$ [21], and oxygen vacancies [22], respectively. The O 1 s peak is broad due to the nonequivalence of surface O^{2-} ions. In addition to the oxygen vacancies, the preexisting oxygen ions in the Zr/CeO$_x$/Pt device can also be verified from the spectra. The presence of more than one peak in the O 1 s spectra may have resulted from
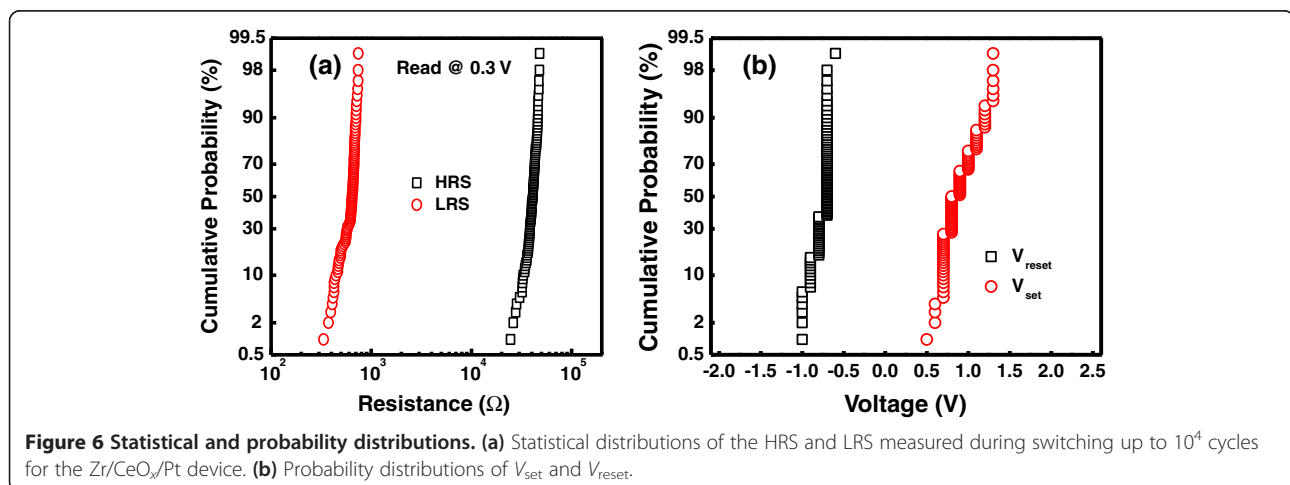

Figure 4 Typical bipolar (*I-V*) curves of resistive switching behavior in Zr/CeO$_x$/Pt devices with different CeO$_x$ layer thicknesses.
(a) 25 nm and (b) 14 nm.

Figure 5 Endurance characteristic of the Zr/CeO$_x$/Pt device during DC sweeping modes up to 10^4 cycles. The read voltage is 0.3 V.
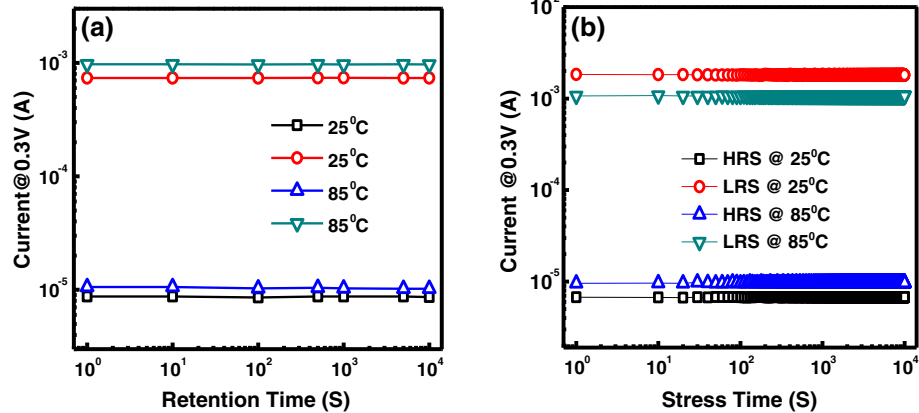
the overlapping of oxygen from surface defects (the nonlattice oxygen ions), CeO$_x$, and Zr-O-Ce components as evident from the deconvoluted curves. The deconvoluted peaks detected at 529.2 to 529.9 and 531.47 eV are ascribed to the lattice oxygen and surface defects, respectively. Nonlattice oxygen ions may exist in the grain boundaries and can move with the help of bias voltage. Interaction between the movable oxygen vacancies and oxygen ions in the presence of an external electric field can play an important role in the RS process [23,24]. Based on the above results, a highly stable and forming-free bipolar resistive switching model can be proposed as shown in Figure 3.

Figure 4a depicts *I-V* bipolar switching characteristics of the Zr/CeO$_x$/Pt device having a CeO$_x$ film thickness of 25 nm under DC sweeping at room temperature. Application of positive DC sweeping voltage gradually activates the device, initially forming a conductive path;

this process is known as 'electroforming' and is similar to defect-induced dielectric soft breakdown. Current gradually increases at the forming voltage (approximately 4 V), and the device is shifted from a high-resistance state (HRS) to a low-resistance state (LRS). At the negative bias of approximately −1.0 V, the current drops abruptly to switch the device from LRS to HRS, known as the reset process. The device returns again to LRS when positive bias exceeds the set voltage ($V_{on} \sim 2.0$ V), and a compliance current of 10 mA is applied to prevent the device from permanent breakdown. The electroforming process usually requires a higher bias and may cause unstable resistance states [8], which make RS characteristics very difficult to modulate. That is why it is valuable to study the resistive switching behavior free from the forming process. In this regard, the thickness of the CeO$_x$ layer was reduced from 25 to 14 nm in the Zr/CeO$_x$/Pt devices. It is noticed that by reducing the thickness of the CeO$_x$ layer, the forming voltage is also reduced. At 14-nm-thick CeO$_x$, the Zr/CeO$_x$/Pt device shows a forming-free behavior, as indicated in Figure 4b. Figure 4b shows the first switching cycle of this device. Initially, the device is in LRS [21], so the first reset process ($V_{off} = -1.4$ V) is required to initialize the device by rupturing the preformed conductive filaments between two electrodes, and the device is switched to HRS [22]. A unique resistive switching behavior can be obtained without any forming process, which is more advantageous for the application point of view [2,22]. Conversely, a positive voltage (V_{on}) of about +1 V is required for the rapid transition of current from HRS to LRS, called the 'set process.' During the set process, oxygen vacancies migrate from the top reservoir (ZrO$_y$ layer) and form conducting filaments [2,4,13,20]. A compliance current of 1 mA was applied to prevent the device from permanent breakdown. An appropriate negative voltage (−0.7 V) is applied to switch the device from LRS back to HRS. During the reset process,
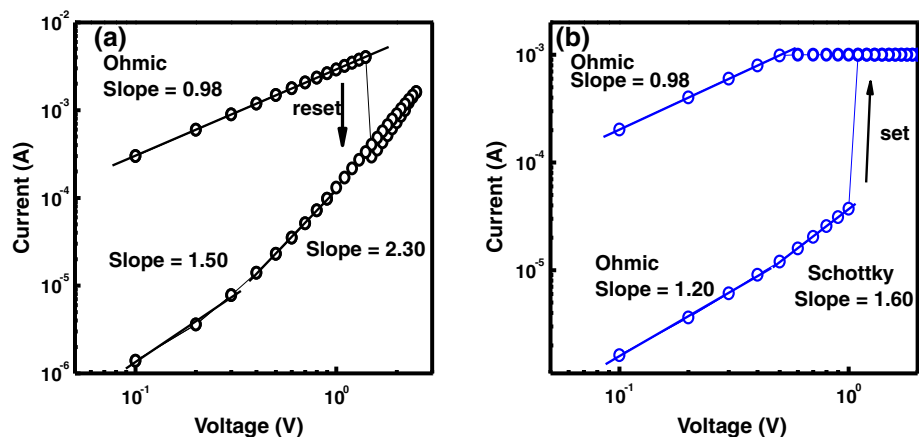

Figure 6 Statistical and probability distributions. (a) Statistical distributions of the HRS and LRS measured during switching up to 10^4 cycles for the Zr/CeO$_x$/Pt device. **(b)** Probability distributions of V_{set} and V_{reset}.

Figure 7 Retention characteristic and nondestructive readout properties. (a) Retention characteristic of the $Zr/CeO_x/Pt$ device. The resistance ratios between HRS/LRS are retained for more than 10^4 s. **(b)** Nondestructive readout properties of both HRS and LRS for 10^4 s.

the conductive filament is ruptured by the reoxidation of oxygen ions [2,13,22,25].

To evaluate the memory switching performance of the $Zr/CeO_x/Pt$ device, endurance characteristics are performed. The memory cell is switched successfully in consecutive 10^4 switching cycles (*I-V* curves) with approximately 40 resistance ratios between HRS and LRS, as shown in Figure 5. Both HRS and LRS are quite stable and no 'set fail' phenomena are observed. Figure 6a shows the statistical distribution of LRS and HRS of the device. Furthermore, the device has very good uniformity of resistance values in both HRS and LRS. Figure 6b depicts the distribution of set (V_{set}) and reset (V_{reset}) voltages for the device, which shows a narrow range of V_{reset} (from −0.5 to −1 V) and V_{set} (from 0.5 to 1.3 V) values. The data retention characteristics of the $Zr/CeO_x/Pt$ device are measured at room temperature (RT) and at 85°C, respectively. As shown in Figure 7a, the HRS and LRS

are retained stable for more than 10^4 s at RT and 85°C with a resistance ratio of approximately 10^2 times at 0.3 V. Hence, suitable read/write durability is obtained. The nondestructive readout property is also verified. As shown in Figure 7b, the two resistance states are stable over 10^4 s under 0.3 V at RT and 85°C, without any observable degradation.

The RS characteristics of the $Zr/CeO_x/Pt$ device are well explained by the model of filamentary conduction mechanism caused by oxygen ions/vacancies [20,26,27]. Due to impulsive interactions, oxygen vacancies tend to distribute themselves in line patterns and separate from each other in the CeO_x film [28]. This phenomenon leads to the formation of independent conducting filaments between electrodes instead of their interconnection network. The abundant oxygen vacancies easily form conducting filaments presented in the CeO_x film, as shown in Figure 3a. The formation mechanism of the conducting filament in

Figure 8 *I-V* curves of the $Zr/CeO_x/Pt$ memory device are displayed in double-logarithmic scale. The linear fitting results in both ON state and OFF state: **(a)** positive-voltage region and **(b)** negative-voltage region. The corresponding slopes for different portions are also shown.

the virgin device could be explained as follows: the oxygen vacancies present in the virgin device can be imagined to be formed partially during the deposition of the nonstoichiometric (oxygen deficient) CeO_2 and partially as a consequence of Zr oxidation. The oxidation of Zr might have increased the concentration of oxygen vacancies in the bulk of the sandwiched nonstoichiometric oxide to such an extent that they formed conductive paths through CeO_x. These conductive filamentary paths composed of oxygen vacancies are somewhat stronger than the filaments that are formed in the subsequent ON states, as indicated by a relatively larger reset power needed for the first reset process (Figure 3b). Such conducting filaments become a cause for the forming-free behavior of the $Zr/CeO_x/Pt$ device. In addition, due to the nonforming process, the current overshoot phenomenon can be suppressed for the following RS [26]. When a negative voltage (V_{off}) is applied on the top electrode, current flows (i.e., the electrons injected from the top electrode) through the conductive filaments that produce local heating at the interface along with the repelled oxygen ions from the ZrO_y layer, causing local oxidization of the filaments at the interface between ZrO_y and CeO_x layers. This oxidization causes the rupture of filaments and the switching of the device to HRS [29], as shown in Figure 3b. Figure 3c depicts the set process; the device can switch from HRS to LRS by applying a positive bias voltage on the Zr top electrode, which causes the drift of oxygen vacancies from the ZrO_y interfacial layer down to CeO_x and the oxygen ions simultaneously upward. The conducting filament consisting of oxygen vacancies is formed. In this RS model, the ZrO_y interfacial layer behaved as an oxygen reservoir in the device. Besides being an oxygen reservoir, the ZrO_y interfacial layer also acts as an ion barrier [30], which may lead to the good endurance property of the $Zr/CeO_x/Pt$ structure.

In order to elucidate the conduction mechanisms of the device, the *I-V* curve is plotted in the double-logarithmic mode, both the positive and negative bias regions, as shown in Figure 8a,b, respectively. The conduction mechanism being responsible for charge transport in the low-voltage region involves ohmic behavior (since $n = 1$), but it is different in the medium- and high-voltage regions for the device, where the conduction behavior can be well described by the space charge-limited current (SCLC) theory [31-36]. Ohmic conduction in LRS is assumed to be caused by the oxygen vacancies which probably provide shallow energy levels below the conduction band edge. The SCLC mechanism is generally observed when the electrode contacts are highly carrier injecting. Due to the formation of an interfacial ZrO_y layer between Zr and CeO_x films, the conduction mechanism in the device behaves according to the SCLC theory since the ZrO_y layer is known to provide electron trapping sites and to control the conductivity by trapping and detrapping.

Conclusions

Resistive switching characteristics of the $Zr/CeO_x/Pt$ memory device were demonstrated at room temperature. The conduction mechanisms for low- and high-resistance states are revealed by ohmic behavior and trap-controlled space charge-limited current, respectively. Oxygen vacancies presented in the CeO_x film and an interfacial ZrO_y layer was formed, as confirmed by XPS and EDX studies. Long retention ($>10^4$ s) at 85°C and good endurance with a memory window of HRS/LRS ≥ 40 were observed. This device has high potential for nonvolatile memory applications.

Authors' contributions
The manuscript was written through the contributions of all authors, MI, CYH, DP, CJH, TLT, JHJ, CAL, UC, AMR, EA, IT, MYN, and TYT. All authors read and approved the final manuscript.

Author details
[1]Department of Electronics Engineering and Institute of Electronics, National Chiao Tung University, Hsinchu 30010, Taiwan. [2]Department of Materials Science and Engineering, National Chiao Tung University, Hsinchu 30010, Taiwan. [3]Department of Physics, Bahauddin Zakariya University, Multan 60800, Pakistan.

References
1. Tseng TY, Sze SM (Eds): *Nonvolatile Memories: Materials, Devices and Applications. Volume 2.* Valencia: American Scientific Publishers; 2012:850.
2. Panda D, Tseng TY: **Growth, dielectric properties, and memory device applications of ZrO₂ thin films.** *Thin Solid Film* 2013, **531**:1–20.
3. Panda D, Dhar A, Ray SK: **Nonvolatile and unipolar resistive switching characteristics of pulsed ablated NiO films.** *J Appl Phys* 2010, **108**:104513.
4. Lin CY, Lee DY, Wang SY, Lin CC, Tseng TY: **Reproducible resistive switching behavior in sputtered CeO₂ polycrystalline films.** *Surf Coat Technol* 2009, **203**:480–483.
5. Liu KC, Tzeng WH, Chang KM, Chan YC, Kuo CC, Cheng CW: **The resistive switching characteristics of a Ti/Gd₂O₃/Pt RRAM device.** *Microelect Reliab* 2010, **50**:670–673.
6. Mondal S, Chen HY, Her JL, Ko FH, Pan TM: **Effect of Ti doping concentration on resistive switching behaviors of Yb₂O₃ memory cell.** *Appl Phys Lett* 2012, **101**:083506.
7. Huang SY, Chang TC, Chen MC, Chen SC, Lo HP, Huang HC, Gan DS, Sze SM, Tsai MJ: **Resistive switching characteristics of Sm₂O₃ thin films for nonvolatile memory applications.** *Solid State Electron* 2011, **63**:189–191.
8. Pan TM, Lu CH: **Switching behavior in rare-earth films fabricated in full room temperature.** *IEEE Trans Electron Devices* 2012, **59**:956–961.
9. Li JGT, Wang Y, Mori T: **Reactive ceria nanopowders via carbonate precipitation.** *J Am Ceram Soc* 2002, **85**:2376–2378.
10. Zhou Q, Zhai J: **Study of the resistive switching characteristics and mechanisms of Pt/CeO₍ₓ₎/TiN structure for RRAM applications.** *Integr Ferroelectr* 2012, **140**:16–22.

11. Panda D, Dhar A, Ray SK: **Non-volatile memristive switching characteristics of TiO$_2$ films embedded with nickel nanocrystals.** *IEEE Trans Nanotechnol* 2012, **11**:51–55.
12. Waser R, Aono M: **Nanoionics-based resistive switching memories.** *Nat Mater* 2007, **6**:833–840.
13. Panda D, Huang CY, Tseng TY: **Resistive switching characteristics of nickel silicide layer embedded HfO$_2$ film.** *Appl Phys Lett* 2012, **100**:112901.
14. Kano S, Dou C, Hadi MS, Kakushima K, Ahmet P, Nishiyama A, Suggi N, Tsutsui K, Kattaoka Y, Natori K, Miranda E, Hattori T, Iwai H: **Influence of electrode materials on CeO$_x$ based resistive switching.** *ECS Trans* 2012, **44**:439–443.
15. Rao RG, Kaspar J, Meriani S, Monte R, Graziani M: **NO decomposition over partially reduced metallized CeO$_2$-ZrO$_2$ solid solutions.** *Catal Lett* 1994, **24**:107–112.
16. Bêche E, Charvin P, Perarnau D, Abanades S, Flamant G: **Ce 3d XPS investigation of cerium oxides and mixed cerium oxide (Ce$_x$Ti$_y$O$_z$).** *Surf Inter Anal* 2008, **40**:264–267.
17. Dittmar A, Hoang DL, Martin A: **TPR and XPS characterization of chromia–lanthana–zirconia catalyst prepared by impregnation and microwave plasma enhanced chemical vapour deposition methods.** *Thermochim Acta* 2008, **47**:40–46.
18. Meng F, Zhang C, Bo Q, Zhang Q: **Hydrothermal synthesis and room-temperature ferromagnetism of CeO$_2$ nanocolumns.** *Mater Lett* 2013, **99**:5–7.
19. Balatti S, Larentis S, Gilmer DC, Lelmini D: **Multiple memory states in resistive switching devices through controlled size and orientation of the conductive filament.** *Adv Mater* 2013, **25**:1474–1478.
20. Wang SY, Lee DY, Huang TY, Wu JW, Tseng TY: **Controllable oxygen vacancies to enhance resistive switching performance in a ZrO$_2$-based RRAM with embedded Mo layer.** *Nanotechnol* 2010, **21**:495201.
21. Geetika K, Pankaj M, Ram SK: **Forming free resistive switching in graphene oxide thin film for thermally stable nonvolatile memory applications.** *J Appl Phys* 2013, **114**:124508.
22. Cao X, Li X, Gao X, Yu W, Liu X, Zhang Y, Chen L, Cheng X: **Forming-free colossal resistive switching effect in rare-earth-oxide Gd$_2$O$_3$ films for memristor applications.** *Appl Phys Lett* 2009, **106**:073723.
23. Kinoshita K, Tamura T, Aoki M, Sugiyama Y, Tanaka H: **Bias polarity dependent data retention of resistive random access memory consisting of binary transition metal oxide.** *Appl Phys Lett* 2006, **89**:03509.
24. Janousch M, Meijer GI, Staub U, Delley B, Karg SF, Andreasson BP: **Role of oxygen vacancies in Cr-doped SrTiO$_3$ for resistance-change memory.** *Adv Mater* 2007, **19**:2232.
25. Panda D, Dhar A, Ray SK: **Nonvolatile and unipolar resistive switching characteristics of pulsed laser ablated NiO films.** *Appl Phys Lett* 2011, **108**:104513.
26. Lin CY, Wang SY, Lee DY, Tseng TY: **Electrical properties and fatigue behaviors of ZrO$_2$ resistive switching thin films.** *J Electrochem Soc* 2008, **155**:H615–H619.
27. Lin CY, Wang SY, Lee DY, Tseng TY: **Ti-induced recovery phenomenon of resistive switching in ZrO$_2$ thin films.** *J Electrochem Soc* 2010, **157**:G167–G169.
28. Esch F, Fabris S, Zhou L, Montini T, Africh C, Fornasiero P, Comelli G, Rosei R: **Electron localization determines defect formation on ceria substrates.** *Science* 2005, **309**:752–755.
29. Chen MC, Chang TC, Huang SY, Chen SC, Hu CW, Tsai CT, Sze M: **Bipolar resistive switching characteristics of transparent indium gallium zinc oxide resistive random access memory.** *Electrochem Solid State Lett* 2010, **13**:H191–H193.
30. Chang WY, Ho YT, Hsu TC, Chen F, Tsai MJ, Wu TB: **Influence of crystalline constituent on resistive switching properties of TiO$_2$ memory films.** *Eletrochem Soild-State Lett* 2009, **12**:H135–H137.
31. Liu Q, Guan W, Long S, Jia R, Liu M, Chen J: **Resistive switching memory effect of ZrO$_2$ films with Zr$^+$ implanted.** *J Appl Phys* 2008, **92**:012117.
32. Guan W, Long S, Liu Q, Liu M, Wang W: **Nonpolar non-volatile resistive switching in Cu doped ZrO$_2$.** *IEEE Trans Elec Lett* 2008, **29**:434–437.
33. Liu Q, Long S, Wang W, Zuo Q, Zhang S, Chen J, Liu M: **Improvement of resistive switching properties in ZrO$_2$-based RRAM with implanted Ti ions.** *IEEE Trans Elec Lett* 2009, **30**:1335–1337.
34. Long S, Cagli C, Lelmini D, Liu M, Sune J: **Analysis and modeling of resistive switching characteristics.** *J Appl Phys* 2012, **111**:074508.
35. Long S, Cagli C, Lelmini D, Liu M, Sune J: **Reset statistics of NiO-based resistive switching memory.** *IEEE Trans Elec Lett* 2011, **32**:1570–1572.
36. Long S, Cagli C, Lelmini D, Liu M, Sune J: **A model for the set statistics of RRAM inspired in the percolation model of oxide breakdown.** *IEEE Trans Elec Lett* 2013, **34**:999–1001.